논문 2006-43SC-6-7

CMOS OTA를 이용한 펄스폭 변조회로

(Pulse Width Modulation Circuits Using CMOS OTAs)

김 훈*, 김 희 준**, 정 원 섭***

(Hoon Kim, Hee-Jun Kim, and Won-Sup Chung)

요 약

본 논문은 CMOS OTA를 이용한 3 개의 PWM 변조기를 제안한다. 이들은 램프 적분기와 전류로 임계전압은 조정할 수 있는 슈미트 트리거로 구성되었다. 개별 소자를 사용해 만든 원형회로는 제안된 PWM 회로들의 시비율이 선형적으로 제어될 수 있음을 보여준다. 제안된 변조기들은 구조가 간단하기 때문에 모노리식 IC로 쉽게 제작할 수 있다.

Abstract

This paper presents three PWM modulators using CMOS OTAs. They consist of a ramp integrator and current-tunable Schmitt triggers. Prototype circuits built using discrete components exhibited that their duty cycles are linearly controllable. The proposed modulators can be easily fabricated in a monolithic IC, because they have a simple structure.

Keywords : 펄스폭 변조, operational transconductance amplifiers, 아날로그 집적회로

I. Introduction

Pulse-width modulation (PWM) is being used for digital audio, communication, and power conversion systems[1]-[3]. A PWM signal can be generated by comparing an information signal with a saw-tooth or triangular waveform. In general, this circuit is readily implemented using an operational amplifier (OP-amp) RC integrator and a Schmitt trigger[4], but can also be obtained using a current conveyor instead of the OP-amp[5]. A derivative PWM signal generator using operational transconductance amplifiers (OTAs) has also been reported[6]. There are other methods of producing a PWM pulse train, such as, with the use of voltage- or current-controlled delay cells[7], [8] and a voltage-controlled phase shifter[9].

This paper presents three PWM modulators using CMOS OTAs and compares their performances. Since the identical OTAs are used as circuit-building blocks, the advantage of the proposed circuits is their integration. Their operating principles are described in section Ⅱ. In section Ⅲ, the pulse periods of the PWM modulators that are considered non-ideal effects and their temperature stabilities are discussed. The experimental results using discrete elements are presented in section Ⅳ.

Ⅱ. Circuit Description

1. Adjustable Schmitt Triggers and Their Second-order Effects

Schmitt triggers with adjustable threshold voltages

---

* 학생회원, 한양대학교 전자전기제어계측공학과
(Department. of Electronics, Electrical, Control, and Instrumentation Engineering, Hanyang University)
** 정회원, 한양대학교 전자컴퓨터공학부
(School of Electronics and Information Engineering Hanyang University)
*** 정회원, 청주대학교 전자정보공학부
(School of Electronics and Information Engineering, Chongju University)
※ 본 논문은 IT-SoC 핵심 설계 인력양성 사업 및 IDEC의 지원으로 수행된 결과임.
접수일자: 2006년 4월

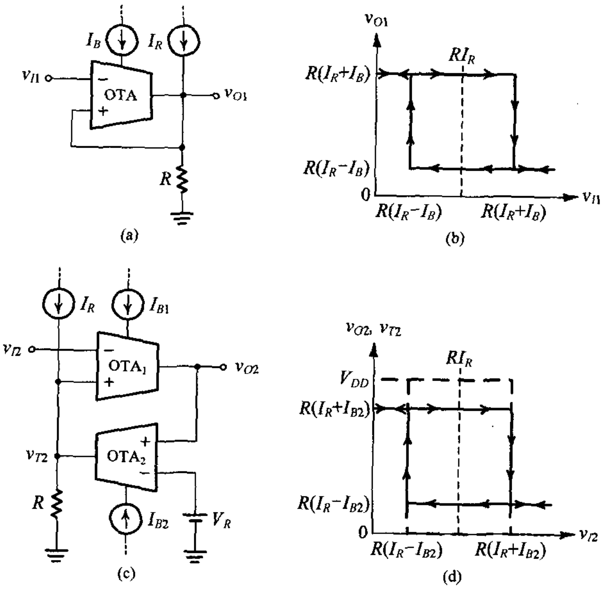

그림 1. (a) 직접 정귀환된 조정 가능한 슈미트 트리거 회로도, (b) 그림 (a) 회로의 이상적인 전달특성, (c) OTA-R 정귀환된 조정 가능한 슈미트 트리거 회로도, (d) 그림 (c) 회로의 이상적인 전달특성.

Fig. 1. (a) Circuit diagram of a direct positive feedback adjustable Schmitt trigger, (b) Ideal transfer characteristics of the circuit in (a), (c) Circuit diagram of a OTA-R positive-feedback adjustable Schmitt trigger, and (d) Ideal transfer characteristics of the circuit in (c).

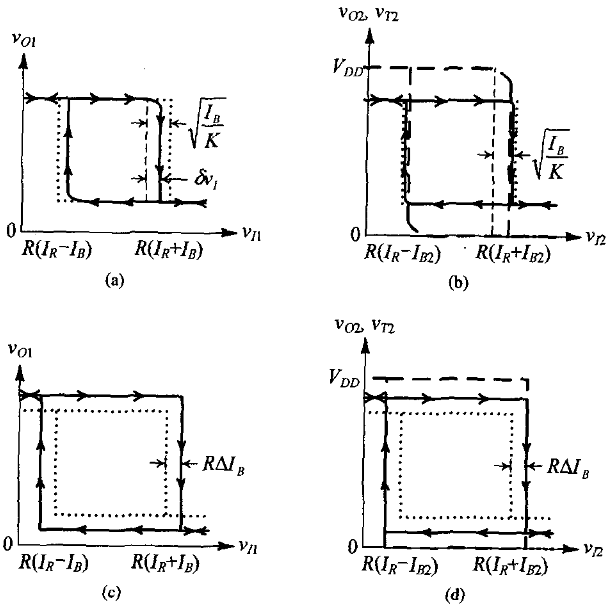

그림 2. OTA 슈미트 트리거의 비이상적인 전달특성: (a) 와 (b) 그림 1(a) 와 (c) 회로의 유한한 입력 선형범위에 대한 영향, (c) 와 (d) 포화전류 증가에 대한 영향.

Fig. 2. Non-ideal transfer characteristics of the OTA Schmitt triggers: (a) and (b) effect on the finite input linear range of the circuit in Fig. 1(a) and (c), and (c) and (d) effect on the saturation current increase.

can be obtained by using OTAs. Circuit diagrams of two OTA Schmitt triggers for a single supply and their transfer characteristics are shown in Fig. 1[10]. The direct positive-feedback Schmitt trigger shown in Fig. 1(a) consists of an OTA and a positive-feedback resistor R. Ideal high and low threshold voltagesof this Schmitt trigger are as follows:

$$V_{TH1} = R(I_R + I_B) \tag{1a}$$

$$V_{TL1} = R(I_R - I_B) \tag{1b}$$

These threshold voltages are linearly adjustable with the dc bias current of the OTA, but are identical tothe output voltage.

The Schmitt trigger shown in Fig. 1(c) has an OTA-R amplifier in a positive-feedback path. This results in the independent of the output voltage from the threshold one. The reference voltage V_R in Fig. 1(c) guarantees the saturation of the OTA_2 at a low saturation level when the output voltage v_{O2} is zero. The short dashed line in Fig. 1(d) represents the transfer characteristics of v_{O2}, and the solid line represents those of the threshold voltage. Ideal threshold voltages are given by

$$V_{TH2} = R(I_R + I_{B2}) \tag{2a}$$

$$V_{TL2} = R(I_R - I_{B2}) \tag{2b}$$

In practice, the threshold voltages deviate from the ideal ones by the finite input linear range,and the saturation current increases over the bias current of an OTA. Fig. 2 shows the non-ideal transfer characteristics of the two Schmitt triggerswhen the OTAs shown in Fig. 3 were used: Fig. 2(a) and (b) show the effect on the finite input linear range of the circuit in Fig. 1(a) and (c), and Fig. 2(c) and (d) show the effect on the saturation current increase.

In Fig. 2(a), the dotted line shows the ideal transfer characteristics of thecircuit in Fig. 1(a) and the solid line shows the transfer characteristics affected by the finite input linear range of the OTA. To estimate such threshold voltage variations, assume that the output voltage v_{O1} is saturated at its high saturation level and the input voltage v_{I1} is increasing into the high threshold voltage level. When the differential input voltage of the OTA reaches the boundary voltage of the input linear range, $\sqrt{I_B/K}$ $(K=(1/2)\mu C_{OX}W/L)$, the OTA begins to operate in the linear region and the threshold voltages decrease. The threshold voltage variation is given by the following equation, using linear approximation:

$$\begin{aligned} v_{O1} &= R(I_R+I_B)-\frac{dv_{o1}}{dv_{I1}}\delta v_{I1} \\ &= R(I_R+I_B)-\frac{G_mR}{G_mR-1}v_{I1} \\ &\quad -\frac{G_mR}{G_mR-1}\left\{\sqrt{\frac{I_B}{K}}-R(I_R+I_B)\right\} \end{aligned} \tag{3}$$

where G_m is the transconductance gain and δv_{I1} is the input voltage variation from the boundary voltage of the input linear range. As v_{I1} increases, v_{O1} falls in terms of (3) until the differential input voltage again reaches $\sqrt{I_B/K}$, after it passes the point at which v_{I1} and v_{O1} are equal. This, in turn, causes the Schmitt trigger to switch to the low saturation level. The deviation of v_{I1} during the OTA operation in the linear region is twice that from the starting point of the linear range to the point at which v_{I1} and v_{O2} are equal. The transconductance gain of the CMOS OTAs shown in Fig. 3 is $\sqrt{2KI_B}$, when its input voltage is zero. Substituting $v_{I1}=v_{O1}$ in (3) and deriving the variation of v_{O1} in the linear region, the high threshold voltagethat is affected by the finite input linear range is given by

$$\begin{aligned} V_{TH1} &= R(I_R+I_B) \\ &\quad -\sqrt{\frac{I_B}{K}}\left(\frac{2R\sqrt{2KI_B}}{2R\sqrt{2KI_B}-1}-1\right) \end{aligned} \tag{4}$$

Fig. 2(b) shows the effect of the finite input linear range of the circuit in Fig. 1(c). The short dashed line shows the transfer characteristics of the output voltage v_{O2}, and the solid line shows those of the threshold voltage v_{T2}. Assume that the output voltage v_O is saturated at its high saturation level and that the input voltage v_{I2} is increasing into the high threshold voltage level. The OTA₁ begins to operate in the linear region when its differential input voltage reaches the boundary voltage of the input linear range, but the OTA₂ is still saturated and thus, the threshold voltage does not change. The output voltage variation in this region is given by, the following equation, using linear approximation:

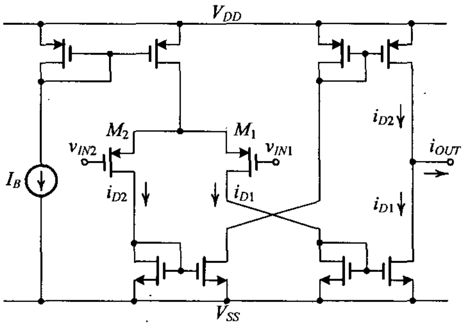

그림 3. CMOS OTA 회로도.
Fig. 3. Circuit diagram of a CMOS OTA.

$$\begin{aligned} v_{O2} &= V_{DD}-G_{m1}R_ov_{I2} \\ &\quad +G_{m1}R_o\left\{\sqrt{\frac{I_{B1}}{K}}-R(I_R+I_{B2})\right\} \end{aligned} \tag{5}$$

where G_{m1} is the transconductance gain of OTA₁. When the decreasing v_{O2} reaches the boundary voltage of the input linear range of OTA₂, $V_R+\sqrt{I_{B2}/K}$, OTA₂ will begin to operate in the linear region. The value of v_{I2} at this point is given by

$$\begin{aligned} v_{I2} &= R(I_R+I_{B2}) \\ &\quad -\sqrt{\frac{I_{B1}}{K}}+\frac{V_{DD}-V_R-\sqrt{I_{B2}/K}}{G_{m1}R_o} \end{aligned} \tag{6}$$

OTA₁ and OTA₂ operate in the linear region until the decreasing v_{T2} reaches the boundary voltage, $v_{I2}-\sqrt{I_{B1}/K}$, that makes OTA₁ again goes to the saturation region. The variation of v_{T2} in this region is given by

$$v_{T2} = R(I_R + I_{B2}) - \frac{G_{m1}G_{m2}R_oR}{G_{m1}G_{m2}R_oR - 1}(v_{I2}) - \frac{G_{m1}G_{m2}R_oR}{G_{m1}G_{m2}R_oR - 1}\left(v_{I2}\Big|_{v_{O2} = V_R + \sqrt{I_{B2}/K}}\right) \tag{7}$$

Substituting v_{T2} with $v_{I2} - \sqrt{I_{B1}/K}$ in (7), the variation of the high-threshold voltage is given by

$$V_{TH2} = R(I_R + I_{B2}) - \frac{\sqrt{\frac{I_{B1}}{K}} - \sqrt{2}RI_{B2}\left(\frac{V_{DD} - V_R}{\sqrt{I_{B2}/K}} - 1\right)}{8K\sqrt{I_{B1}I_{B2}}R_oR - 1} \tag{8}$$

As a result, the OTA-R positive-feedback Schmitt trigger is insensitive to the finite input linear range of an OTA, compared withthe direct positive-feedback Schmitt trigger.

The effect of the OTA's saturation current increase, which consisted of the circuit in Fig. 1(a) and (c), is illustrated in Fig. 2(c) and (d), respectively. The ideal saturation current of the OTA should be equal to the current value of its dc bias. The non-ideal saturation current slightly increased, however, with the channel length modulation of the MOSFETs, which consisted of the current mirrors of the OTA. Assuming that the simple current mirror was employed and the MOSFETs were perfectly matched, the non-ideal saturation current of the OTA I_O would be as follows:

$$\begin{aligned} I_O &= \left\{1 + \frac{\lambda(V_{DS2} - V_{DS1})}{1 + \lambda V_{DS1}}\right\}I_B \\ &\approx \{1 + \lambda(V_{DS2} - V_{DS1})\}I_B \end{aligned} \tag{9}$$

where λ is the channel length modulation parameter, V_{DS1} is the drain-to-source voltage of the diode connect MOSFET, V_{DS2} is that of the other one, and I_B is the bias current of the OTA. The equation (9) shows that ΔI_B in Fig. 2(c) and (d) is $\lambda(V_{DS2} - V_{DS1})I_B$.

2. Saw-tooth Carrier Based PWM Modulator

Fig. 4 shows a circuit diagram of the saw-tooth carrier based PWM modulator operating on a single supply. It consists of the direct positive-feedback Schmitt trigger, an integrator composed of the current source I_T and the capacitor C_1, the inverter, the n-MOSFET switch M_1, and a comparator composed of OTA2 and its output resistance. The waveforms associated with this modulatorare shown in Fig. 5. To see how the modulatoroperates, assume that the output voltage of the Schmitt trigger v_T is at its high saturation level, $R_1(I_R + I_B)$, thus opening the n-MOSFET switch M_1 and charging the capacitor C_1 with a slope of I_T/C_1. The input voltage of the Schmitt trigger v_I continues to increase until v_I reaches its high-threshold voltage, $V_{TH} = R_1(I_R + I_B)$. During the interval T_1, the following equation is obtained, from Fig. 5,

$$\frac{R_1(I_R + I_B) - R_1(I_R - I_B)}{T_1} = \frac{I_T}{C_1} \tag{10}$$

Rearranging the equation gives

$$T_1 = 2C_1R_1\frac{I_B}{I_T} \tag{11}$$

When v_I reaches V_{TH}, v_T will switch to the low saturation level, $R_1(I_R - I_B)$. At this instant, switch M_1 shall close. This, in turn, will exponentially discharge capacitor C_1 via switch M_1. Since the on-resistance of M_1 is very small, interval T_2 can be neglected compared to T_1. The period of the saw-tooth waveform T_{s1} is

$$T_{s1} \approx 2C_1R_1\frac{I_B}{I_T} \tag{12}$$

Note that the period of the saw-tooth waveform is directly proportional to the currents ratio, $\underline{I_B}$, so their temperature-dependent terms are cancelled out. Neglecting the temperature coefficients of C_1 and

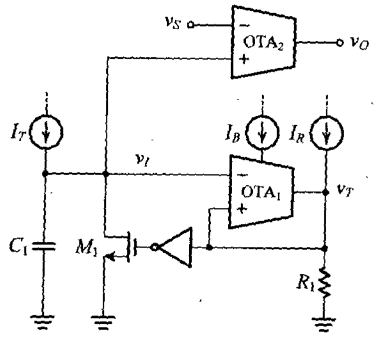

그림 4. 톱니파 캐리어 PWM 회로도.

Fig. 4. Circuit diagram of the saw-tooth carrier PWM.

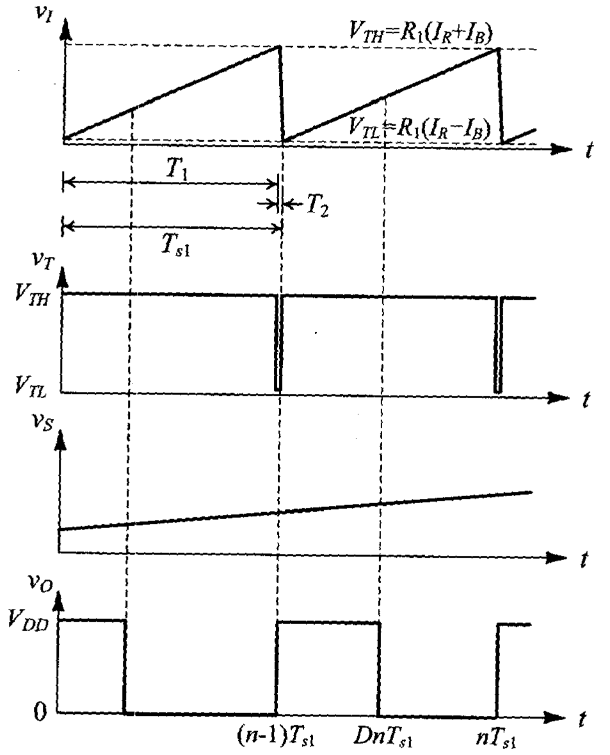

그림 5. 그림 4 회로의 다양한 마디에서 이상적인 전압 파형.

Fig. 5. Ideal voltage waveforms at various nodes of the circuit in Fig. 4.

R_1, the period is stable against temperature variations.

The PWM signal is periodically generated by comparing the signal voltage v_S with the saw-tooth wave voltage v_I. From the waveform of the PWM signal v_O shown in Fig. 5, the duty cycle D is given by

$$D=\frac{v_S(DnT_{s1})}{2R_1I_B}+\frac{1}{2}\left(1-\frac{I_R}{I_B}\right) \tag{13}$$

3. Triangular Carrier Based PWM Modulator

A circuit diagram of the triangular carrier based PWM modulator is shown in Fig. 6. It consists of the OTA-R positive-feedback Schmitt trigger, an OTA-C integrator, and a comparator composed of OTA_4 and its output resistance. The waveforms associated with this modulator are shown in Fig. 7. To see how the modulator operates, assume that the output voltage of Schmitt trigger v_{O1} is at its high saturation level, V_{DD}, thus saturating OTA_3 and charging capacitor C_2 with a slope of I_{B3}/C_2. The input voltage of Schmitt trigger v_I continues to increase until v_I reaches the high-threshold voltage, $V_{TH}=R_2(I_R+I_{B2})$. Interval T_1 is given by the following equation, from Fig. 7:

$$T_1=2C_2R_2\frac{I_{B2}}{I_{B3}} \tag{14}$$

When v_I reaches V_{TH}, v_T will switch to the low saturation level, $R_2(I_R-I_{B2})$, which is much lower than V_R and this, in turn, will reverse the output current of the OTA_3. Thus, v_I starts to decrease with a slope of $-I_{B3}/C_2$. Interval T_2 is given by

$$T_2=2C_2R_2\frac{I_{B2}}{I_{B3}} \tag{15}$$

Combining (14) and (15), the period of the triangular waveform T_{s2} is

$$T_{s2}=4C_2R_2\frac{I_{B2}}{I_{B3}} \tag{16}$$

Similarly to the equation (12), the temperature-dependent terms of the bias currents, I_{B2} and I_{B3}, are cancelled out, and the period is stable against temperature variations.

The PWM signal is periodically generated by comparing the signal voltage v_S with the triangular wave voltage v_I. During interval D_1T_{s2}, the following equation is obtained from the waveform of the PWM signal v_O in Fig. 6:

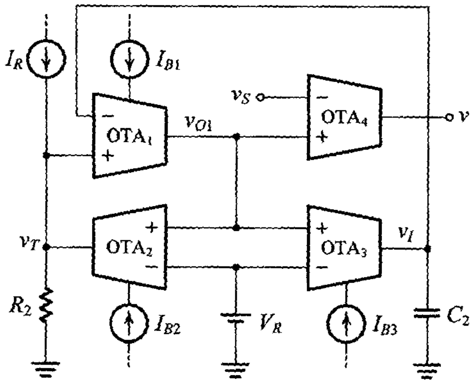

그림 6. 삼각파 캐리어 PWM 회로도.
Fig. 6. Circuit diagram of the triangular carrier PWM.

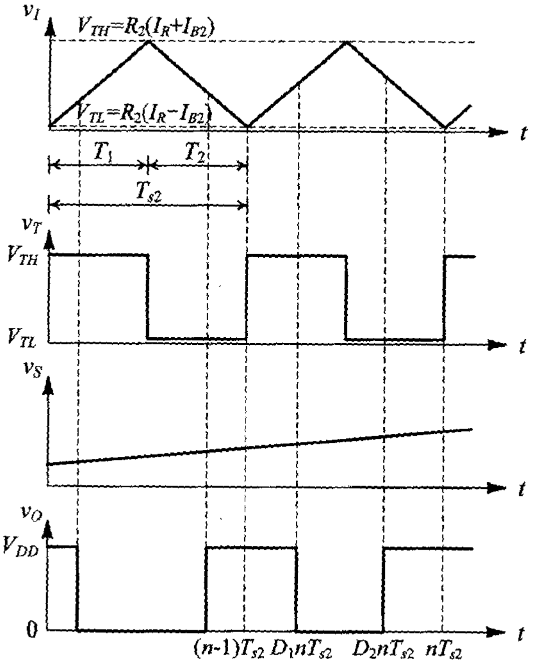

그림 7. 그림 6 회로의 다양한 마디에서 이상적인 전압 파형.
Fig. 7. Ideal voltage waveforms at various nodes of the circuit in Fig. 6.

$$\frac{v_s(D_1 n T_{s2}) - R_2(I_R - I_B)}{D_1 n T_{s2}} = \frac{I_{B3}}{C_2} \tag{17}$$

from which is obtained:

$$D_1 n T_{s2} = \frac{C_2}{I_{B3}}\{v_S(D_1 n T_{s2}) - R_2(I_R - I_B)\} \tag{18}$$

Similarly, during $(1-D_2)nT_{s2}$ the following is obtained:

$$\frac{v_S(D_2 n T_{s2}) - R_2(I_R - I_B)}{(1-D_2)n T_{s2}} = \frac{I_{B3}}{C_2} \tag{19}$$

from which is obtained:

$$(1-D_2)nT_{s2} = \frac{C_2}{I_{B3}}\{v_S(D_2 n T_{s2}) - R_2(I_R - I_B)\} \tag{20}$$

From (18) and (20), the duty cycle D is given by the following equation, assuming that $v_S(D_1 n T_{s2}) = v_S(D_2 n T_{s2}) = v_S(DnT_{s2}/2)$:

$$D = \frac{v_S(DnT_{s2}/2}{2R_2 I_{B2}} + \frac{1}{2}\left(1 - \frac{I_R}{I_{B2}}\right) \tag{21}$$

4. Current-sensing PWMModulator

Fig. 8 shows a circuit diagram of a current sensing PWM modulator. It consists of the two OTA-R positive-feedback Schmitt triggers, an integrator composed of the current source I_T and a capacitor C_3, and the n-MOSFET switch M_3. The waveforms associated with this modulator are shown in Fig. 9. The generation principle of the saw-tooth wave voltage v_I is similar to that of the circuit in Fig. 4. The period of the saw-tooth waveform T_{s3} is given by

$$T_{s3} = 4C_3 R_3 \frac{I_B}{I_T} \tag{22}$$

The duty cycle is given by

$$D = \frac{1}{2}\frac{i_A}{I_B} \tag{23}$$

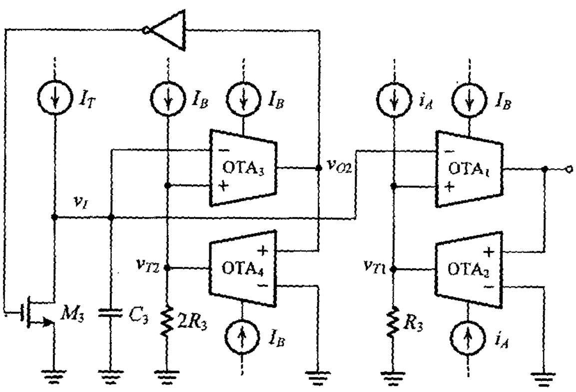

그림 8. 전류-센싱 PWM 회로도.
Fig. 8. Circuit diagram of a current-sensing PWM.

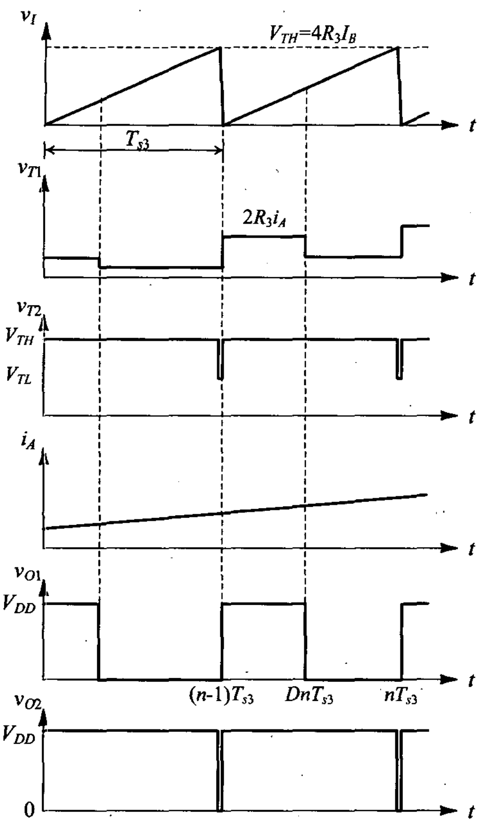

그림 9. 그림 8 회로의 다양한 노드에서 이상적인 전압 파형.

Fig. 9. Ideal voltage waveforms at various nodes of the circuit in Fig. 8.

Note that the period and the duty cycle are directly proportional to the currents ratio, so their temperature-dependent terms are balanced out.

Comparing the theoretical periods, the triangular carrier based PWM modulator needs two times the integration slope required by the other modulators, with the same passive components.In the third PWM modulator, letting v_{T1} be fixed and changing v_{T2}, the pulse frequency modulation (PFM) can be realized.

Ⅲ. Accuracy and Stability

1. Accuracy of the Period and the Duty Cycle

The sources of error are the threshold voltage variations of the Schmitt triggers due to the finite input linear range, the saturation current increase, and the finite switching delay due to the slew rate of the amplifiers. The non-ideal waveforms of the circuit in Fig. 4 are shown in Fig. 10. Assume that the errors of the high- and low-threshold voltages are identical and that the current source I_T is constant. The main source of error at interval T_1 is the variation of the threshold voltage. Thus, the non-ideal T_1 is given by the following equation, with reference to (4) and (9):

$$\begin{aligned} T_1 &= 2C_1R_1\frac{I_B}{I_T}\left\{1+\frac{\Delta I_B}{I_B}\right\} \\ &+2C_1R_1\frac{I_B}{I_T}\left\{\sqrt{\frac{I_B}{K}}-2R_1I_Ba\right\} \end{aligned} \tag{26}$$

where

$$a=\frac{\sqrt{2}}{2R_1\sqrt{2KI_B}-1}$$

At interval T_2, the time delay is caused by the slew rate of the Schmitt trigger and the finite discharging time of the capacitor C_1. Accounting for these factors, T_2 is given by

$$\begin{aligned} T_2 &= 2\frac{V_{TH}-V_{TL}}{S_R}+C_1R_{on}\ln\frac{V_{TH}}{V_{TL}} \\ &\approx 2\frac{2I_B}{S_R}+C_1R_{on}\ln\frac{I_R+I_B}{I_R-I_B} \end{aligned} \tag{27}$$

where S_R is the slew rate of the Schmitt trigger and R_{on} is the on-resistance of the n-MOSFET switch. Considering the above errors, period T_{s1} is expressed as:

$$\begin{aligned} T_{s1} &= 2C_1R_1\frac{I_B}{I_T}\left(1+\frac{\Delta I_B}{I_B}+\sqrt{\frac{I_B}{K}}\right) \\ &-2C_1R_1\frac{I_B}{I_T}\left(2R_1I_Ba\right) \\ &+2C_1R_1\frac{I_B}{I_T}\frac{2I_T}{C_1S_R}\left(1+\frac{\Delta I_B}{I_B}\right) \\ &+2C_1R_1\frac{I_B}{I_T}\frac{R_{on}I_T}{2R_1I_B}\ln\frac{\mathrm{I_R}+\mathrm{I_B}}{\mathrm{I_R}-\mathrm{I_B}} \end{aligned} \tag{28}$$

If $I_R=I_B$ or R_{on} is significantly small, the last term in (28) may be expressed as $(5R_{on}I_T)/(2R_1I_B)$. The equation (28) shows that T_{s1} increases over the theoretical value due to the slew rate and R_{on} and decreases with the amplifier gain.

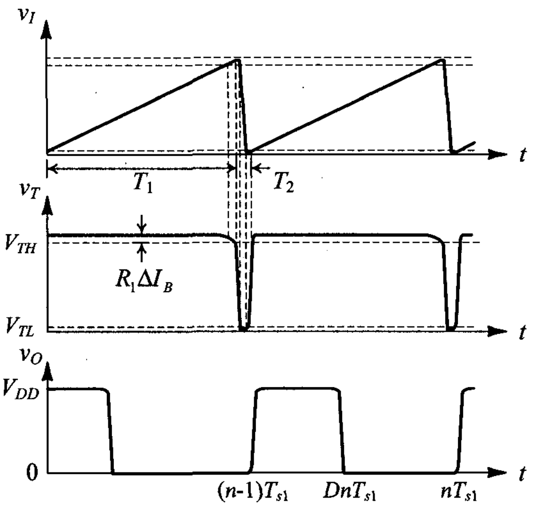

그림 10. 그림 4 회로의 비이상적인 전압 파형.
Fig. 10. Non-ideal voltage waveforms of the circuit in Fig. 4.

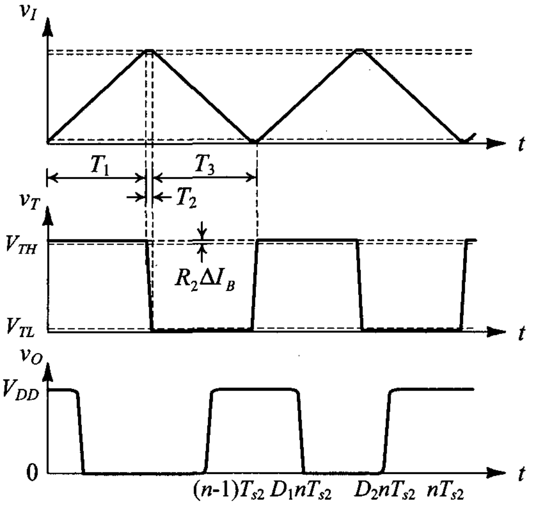

그림 11. 그림 6 회로의 비이상적인 전압 파형.
Fig. 11. Non-ideal voltage waveforms of the circuit in Fig. 6.

The duty cycle affected by the slew rate of OTA₂ is given by the following equation, neglecting the error of T_{s1}:

$$D = \frac{v_S(DnT_s)}{2R_1 I_B} + \frac{1}{2}\left(1 - \frac{I_R}{I_B}\right) + \frac{V_{DD} I_T}{2C_1 R_1 I_B}\frac{C_{o2}}{I_{B2}} \tag{29}$$

where C_{o2} is the parasitic capacitance of the output of OTA₂, and I_{B2} is the bias current of OTA₂.

Fig. 11 shows the non-ideal waveforms of the circuit in Fig. 6. The source of error during interval T_1 is the saturation current increase in the OTAs and the variation of the threshold voltage, and the source of error during interval T_2 is the slew rate of the Schmitt trigger. Interval T_3 equals the sum of T_1 and T_2. Considering these effects, the period T_{s2} is as follows:

$$\begin{aligned} T_{s2} = {} & 4C_2R_2\frac{I_{B2}}{I_{B3}}\left(\frac{1+\Delta I_{B2}/I_{B2}}{1+\Delta I_{B3}/I_{B3}}\right) \\ & -4C_2R_2\frac{I_{B2}}{I_{B3}}\left(\sqrt{I_{B1}/K} - \sqrt{2}b\right)d \\ & +4C_2R_2\frac{I_{B2}}{I_{B3}}\left\{\frac{I_{B3}}{C_2S_R}\left(1+\frac{\Delta I_{B2}}{I_{B2}}\right)\right\} \end{aligned} \tag{30}$$

where

$$b = R_2 I_{B2}\left(\frac{V_{DD} - V_R}{\sqrt{I_{B2}/K}} - 1\right)$$

$$c = 8K\sqrt{I_{B1}I_{B2}}R_oR_2$$

$$d = \frac{1}{c-1}$$

S_R = the slew rate of the Schmitt trigger.

The equation (30) shows that T_{s2} increases with the slew rate and decreases withthe gain of the amplifier and V_R. The non-ideal duty cycle which affected by the slew rate of OTA₄ is given by

$$D = \frac{v_S(DnT_s/2)}{2R_2 I_{B2}} + \frac{1}{2}\left(1 - \frac{I_R}{I_{B2}}\right) + \frac{V_{DD} I_{B3}}{4C_2 R_2 I_{B2}}\frac{C_{o4}}{I_{B4}} \tag{31}$$

where C_{o4} is the parasitic capacitance of the output of OTA4 and I_{B4} is the bias current of OTA4.

In the circuit in Fig. 8, the possible minimum v_O, $V_{DD} - \sqrt{2}R_oI_{B1}$, is always greater than $\sqrt{I_{B2}/K}$. I_{B1} is the bias current of OTA₁ and I_{B2} is that of OTA₂, because the possible maximum v_I is $R_3(I_R + I_{B2})$. Thus, OTA₂ maintains its high saturation level until OTA₁ switches to the low saturation level. As soon as OTA₁ switches, OTA₂ also switches to the low saturation level. Similar to

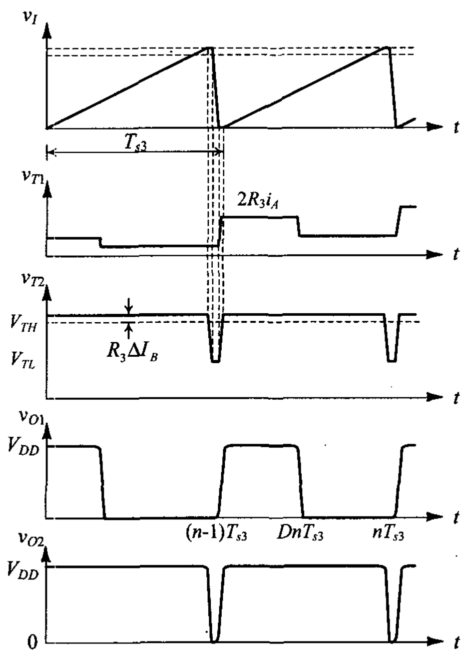

그림 12. 그림 8 회로의 비이상적인 전압 파형.
Fig. 12. Non-ideal voltage waveforms of the circuit in Fig. 8.

the behavior of the saw-tooth carrier based PWM modulator, except for the effect of the input linear range of the OTA, the non-ideal period of the circuit in Fig. 8 is given by the following equation, from Fig. 12:

$$T_{s3} = 4C_3R_3\frac{I_B}{I_T}\left(1+\frac{\Delta I_B}{I_B}+\frac{5R_{on}I_T}{4R_3I_B}\right) + 4C_3R_3\frac{I_B}{I_T}\frac{2I_T}{C_3S_R}\left(1+\frac{\Delta I_B}{2I_B}\right) \quad (32)$$

where S_R is the slew rate of the Schmitt trigger and R_{on} is the on-resistance of the n-MOSFET switch. The equation (32) shows that T_{s3} increases with the slew rate and R_{on}. The non-ideal duty cycle which changed by the slew rate of the Schmitt trigger is given by

$$D=\frac{1}{2}\frac{i_A}{I_B}\left(1+\frac{V_{DD}I_T}{2C_3R_3S_Ri_A}\right) \quad (33)$$

2. Temperature Stability

The temperature stability of the signal-generating period of the modulators depends on the temperature coefficient (TC) of the charge and discharge currents, switching delays, and Schmitt trigger thresholds, as well as on the passive components. To simplify this discussion, assume that the current sources and the passive components are ideal, and neglect the TC of the slew rate. Thus, the temperature-dependent terms shown in (28), (30), and (32), are the conductivity parameter K and the on-resistance of MOSFETs. The TC of the on-resistance is given by

$$\frac{1}{R_{on}}\frac{\partial R_{on}}{\partial T}=-\frac{1}{K}\frac{\partial K}{\partial T}-\frac{1}{V_{GS}-V_{th}}\frac{\partial V_{th}}{\partial T} \quad (34)$$

Differentiating (28), (30) and (32), the temperature stabilities of the proposed modulators are as follows:

$$\begin{aligned}\frac{1}{T_{s1}}\frac{\partial T_{s1}}{\partial T} &= (R_1I_Ba+R_1I_Ba^2)\frac{1}{K}\frac{\partial K}{\partial T}\\ &\quad -\left(\frac{1}{2}\sqrt{\frac{I_B}{K}}+\frac{R_{on}I_T}{2R_1I_B}\right)\frac{1}{K}\frac{\partial K}{\partial T}\\ &\quad -\frac{R_{on}I_T}{2R_1I_B}\frac{1}{V_{GS}-V_{th}}\frac{\partial V_{th}}{\partial T}\end{aligned} \quad (35a)$$

$$\begin{aligned}\frac{1}{T_{s2}}\frac{\partial T_{s2}}{\partial T} &= \left(\sqrt{\frac{I_{B1}}{K}}+bd\frac{R_2I_{B2}}{\sqrt{2}}\right)\frac{d}{2K}\frac{\partial K}{\partial T}\\ &\quad +\left(\sqrt{\frac{I_{B1}}{K}}+\sqrt{2}b\right)\frac{c\cdot d^2}{K}\frac{\partial K}{\partial T}\end{aligned} \quad (35b)$$

$$\begin{aligned}\frac{1}{T_{s3}}\frac{\partial T_{s3}}{\partial T} &= -\frac{5R_{on}I_T}{4R_3I_B}\frac{1}{K}\frac{\partial K}{\partial T}\\ &\quad -\frac{5R_{on}I_T}{4R_3I_B}\frac{1}{V_{GS}-V_{th}}\frac{\partial V_{th}}{\partial T}\end{aligned} \quad (35c)$$

To compare the temperature stability of the modulators, let all the values in (35) be equal to one except that of $V_R = 0.5$, $R_1 = R_2 = R_3 = 10$, and let $R_o = 100$. Then, their TCs will be 70 ppm/°C, 17 ppm/°C, and 687 ppm/°C, respectively. This reveals that the second PWM modulator is the most stable of the proposed modulators against temperature drift. In (35c), there is no term related to the finite input linear range and only R_{on} terms exist. In general, R_{on} is very small. Thus, the TC of the third PWM modulator may be much less than the estimated value.

Ⅳ. Experiment Results and Discussion

The prototype PWM modulatorsshown in Fig. 4, 6 and 8 were built using discrete components. The MOSFET arrays MC14007 were used for the CMOS OTAs shown in Fig. 3. The passive component values with 5% tolerance were adopted as follows: $C_1 = C_3 = 2.3$ nF, $C_2 = 2$ nF, $R_1 = 3$ kΩ, and $R2 = R_3 = 1$ kΩ. The values of the current sources in Fig. 4 and 8 were set at 0.5 ㎃, and those in Fig. 6, at 1 ㎃,to make the oscillation frequency 100 kHz. The signal current i_A in Fig. 8 was produced by a voltage-to-current converter using LM324, a 1-kΩ resistor, and current mirrors. The supply voltage V_{DD} was +5 V and the reference voltage V_R was +2.5 V.

Fig. 13 to 15 show the measured voltage waveforms of the circuit in Fig 4, 6 and 8, in turn: from the top trace, the output voltage of the integrator, the threshold voltage of the Schmitt trigger, the PWM voltage, and the waveform-shaped PWM voltage. Since the parasitic capacitances and the input linear range of the OTAs built using MC14007 were relatively large and wide, the rising and falling time of the PWM waveforms generated were large, similar to those in the figures. Thus, they had to be shaped into a sharp rectangular wave with the two inverters connected in cascade. Observing the threshold voltage waveforms, one can see the non-ideal effects due to the finite input linear range of the OTAs such as those mentioned in subsection A of section II.

Fig. 16 shows the pulse-width modulated waveforms of the proposed modulators when their input signals were 10 kHz sine wave. Fig. 16 shows that the proposed modulators give the changed pulse width as the magnitude of the input signal.

Fig. 17 shows the measured duty cycle D of the modulators with varying the input signals. This figure shows that the duty cycles of the proposed modulator were linearly controlled by the input signal variations. The duty cycle change was nonlinear,

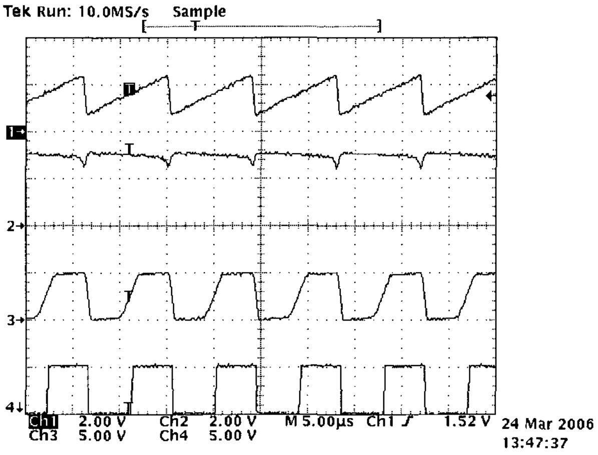

그림 13. 그림 4 회로의 측정된 전압 파형.

Fig. 13. Measured voltage waveforms of the circuit in Fig. 4.

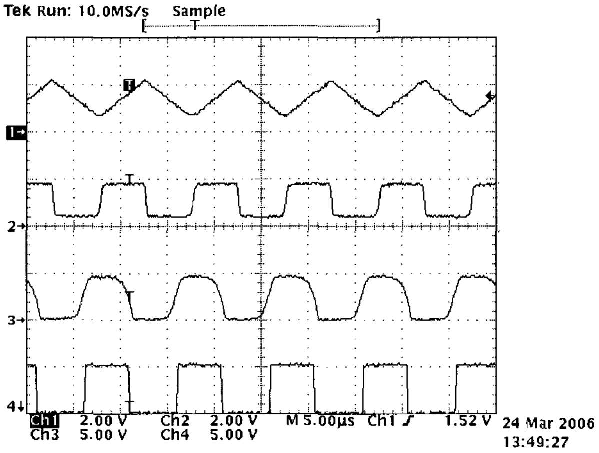

그림 14. 그림 6 회로의 측정된 전압 파형.

Fig. 14. Measured voltage waveforms of the circuit in Fig. 6.

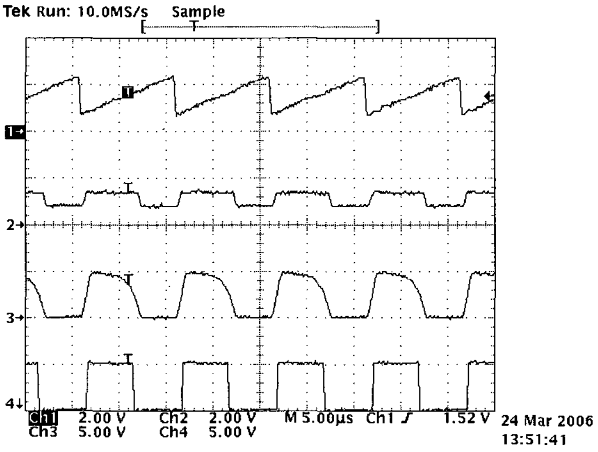

그림 15. 그림 8 회로의 측정된 전압 파형.

Fig. 15. Measured voltage waveforms of the circuit in Fig. 8.

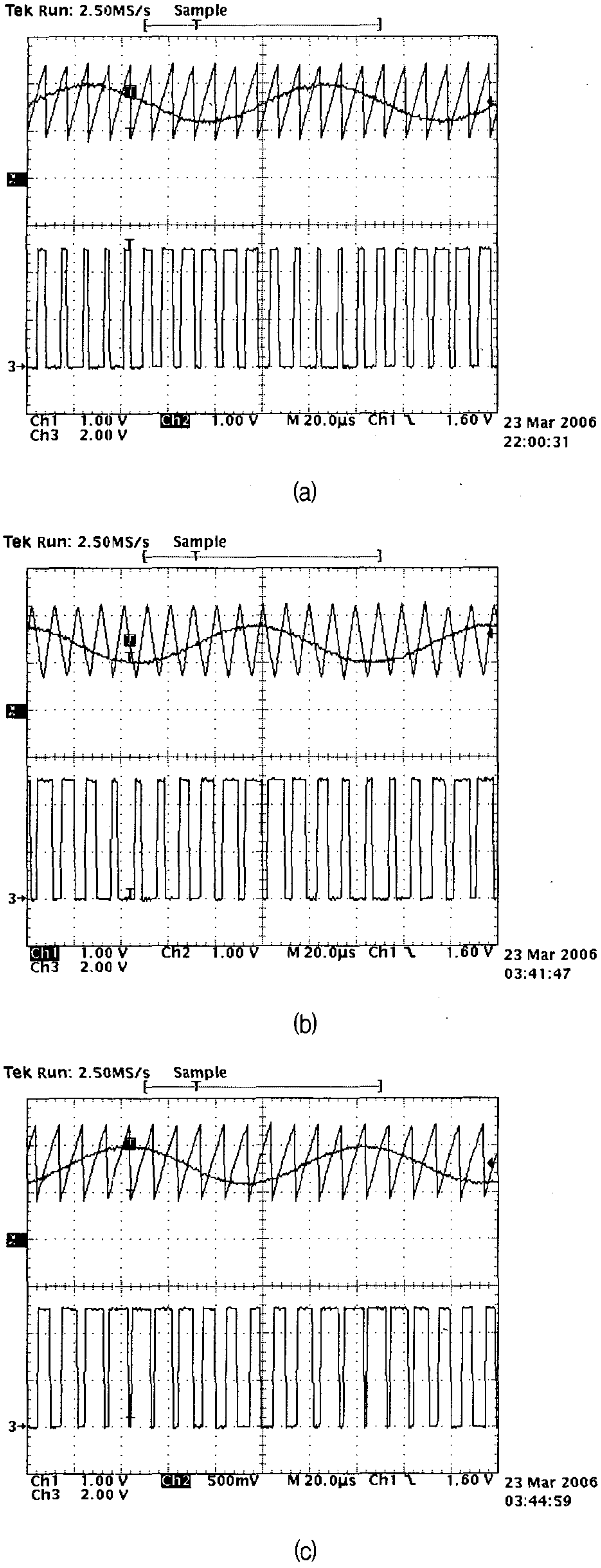

(a)

(b)

(c)

그림 16. 정현파 입력에 대해 측정된 PWM 파형들.

Fig. 16. Measured PWM waveforms for s sinusoidal input.

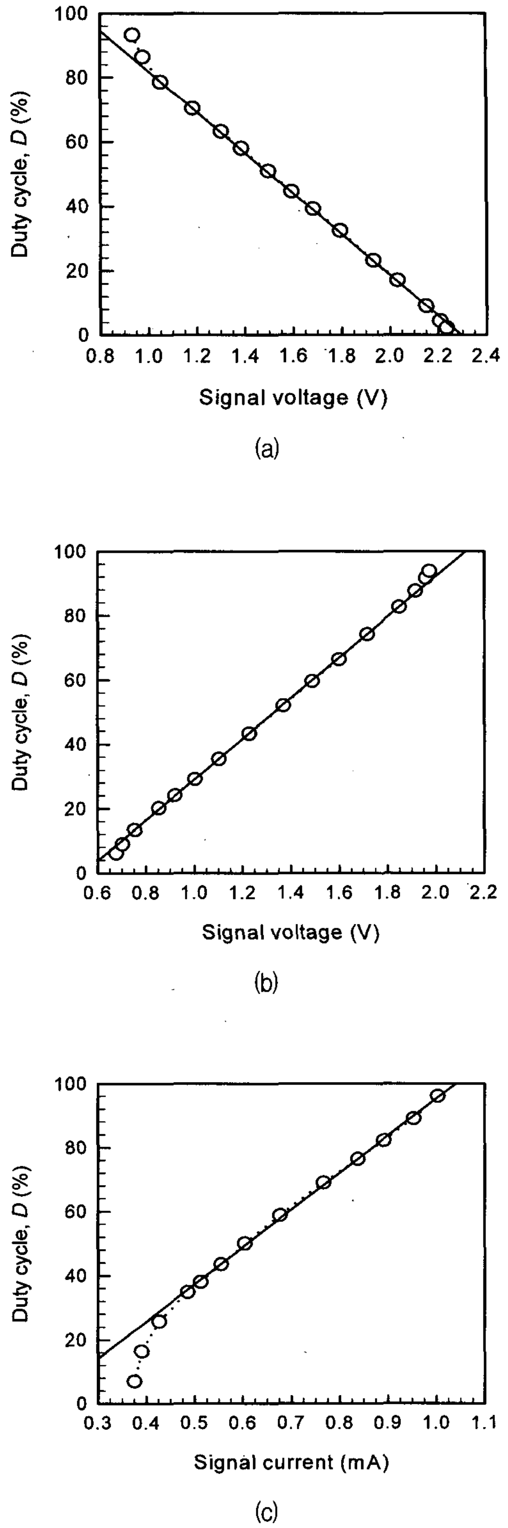

(a)

(b)

(c)

그림 17. 측정된 시비율 *D* 대 입력 신호.

Fig. 17. Measured duty cycle *D* versus the input signals.

however, at the vicinity of the duty cycle, which was 0 and 100%, because the edge of the PWM waveform generated was not sharp, similar to the third trace in Fig. 13-15.

V. Conclusion

Three PWM modulators using CMOS OTAs were described in this paper. Their design principle and circuit configurations are simple and theirestimated temperature stabilities are relatively low. They can be fabricated into a monolithic IC form by scaling their component values. The experiment results presented demonstrate that the duty cycles of the modulators linearly change with their input signals. In addition, the current-sensing modulator can be used as a PFM circuit. The proposed modulators can be applied to analog-to-digital and power conversion systems.

참 고 문 헌

[1] W. Mathis, "Nonlinear systems and communications systems," *Proc. IEEE TELSIKS 2001 Conf.*, vol. 1, pp. 293-296, Sept. 2001.

[2] M. S. Roden, *Analog and Digital Communication Systems 4th Ed.*, Prentice-Hall, Inc., 1996.

[3] D. Maksimovi and S. uk, "A unified analysis of PWM converters in discontinous modes," *IEEE Trans. Power Electronics*, vol. 6, pp. 476-490, July 1991.

[4] D. H. Sheingold, *Nonlinear Circuits Handbook*, Analog Devices, Inc. 1974.

[5] M. Siripruchyanun, P. Wardkein, and W. Sangpisit, "A simple pulse width modulator using current conveyor," *Proc. IEEE TENCON 2000 Conf.*, vol. 1, pp. 452-457, Sept. 2000.

[6] M. Siripruchyanun and P. Wardkein, "A fully independently adjustable, integrable simple current controlled oscillator and derivative PWM signal generator," *IEICE Trans. Funds.*, vol. E86-A, no. 12, pp. 3119-3126, Dec. 2003.

[7] A. Djemouai, M. Sawan, and M. Slamai, "New CMOS integrated pulse width modulator for voltage conversion applications," *Proc. IEEE ICECS 2000 Conf.*, vol. 1, pp. 116-119, Dec. 2000.

[8] J.-J. Chen, H.-Y. Lin, Y.-T. Lin, and W.-Y. Chung, "Integrated pulse-width-modulation circuit using CMOS processes," *Proc. IEEE PESC* 04 Conf., vol. , pp. 1356-1358, June 2004.

[9] Y. Zheng and C. E. Saavedra, "Pulse width modulator using a phase-locked loop variable phase shifter," *Proc. IEEE ISCAS 2005 Conf.*, vol. 4, pp. 3639-3642, May 2005.

[10] K. Kim, H.-W. Cha, and W.-S. Chung, "OTA-R Schmitt trigger with independently controllable threshold and output voltage levels," *Electronics letters*, vol. 33, no. 13, pp. 1103-1105, June 1997.

저 자 소 개

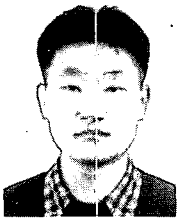

김 훈(학생회원)
2003년 청주대학교 정보통신공학부 공학사
2005년 청주대학교 전자공학과 공학석사
2005년~현재 한양대학교 전자전기제어계측공학과 박사과정
<주관심분야 : 아날로그 IC 설계, 센서 신호처리, DC-DC 컨버터>

정 원 섭(정회원)
1977년 한양대학교 전자통신공학과 공학사
1979년 한양대학교 전자통신공학과 공학석사
1987년 일본 정강대학교 전자과학연구과 공학박사
1986년~현재 청주대학교 전자정보공학부 교수
<주관심분야 : 전류모드 아날로그 신호처리, 센서 신호처리>

김 희 준(정회원)
1976년 한양대학교 전자공학과 공학사
1978년 한양대학교 전자공학과 공학석사
1986년 일본 큐슈대학교 전자공학과 공학박사
1991년~1992년 Virginia공대 방문교수
1987년~현재 한양대학교 전자컴퓨터공학부 교수
<주관심분야 : DC-DC 컨버터, MCM IC, 아날로그 CMOS IC 설계>